Spatial Clustering Analysis with Spectral Imaging-based Single-Step Multiplex Immunofluorescence (SISS-mIF)

Tomohiko Nakamura[#1], Noe Kaneko[#1], Towako Taguchi[#2], Kenji Ikeda[1], Moe Sakata[1], Miori Inoue[2], Tetsuro Kuwayama[1], Hirokazu Tatsuta[1], Iichiroh Onishi[2], Morito Kurata[2], and Kazuhiro Nakagawa[*1]

[1]*Life Science Technology Research & Development Dept., Application Technology Research & Development Div., Technology Development Laboratories, Sony Corporation*
[2]*Department of Comprehensive Pathology, Graduate School of Medical and Dental Sciences, Tokyo Medical and Dental University*

[#]These authors contributed equally: T.N., N.K., and T. T.
[*]To whom correspondence and request for materials should be addressed:
Kazuhiro Nakagawa, E-mail: Kazuhiro.Nakagawa@sony.com

Abstract

Precision medicine, anchored in spatial biology, is essential for the accurate diagnosis of cancer and prediction of drug responses. We have introduced the Spectral Imaging-based Single-Step Multiplex Immunofluorescence (SISS-mIF) technique, which leverages hyperspectral imaging to simultaneously capture fluorescence spectra. This approach automatically optimizes tissue autofluorescence spectra for each image, facilitating the use of fluorescent direct-labeled antibodies for multicolor staining in a single step. Unlike conventional methods, images are outputted as antibody counts rather than fluorescence intensity, allowing for consistent comparisons under different imaging conditions. We demonstrate that this technique allows for identical cell detection of CD3, CD5, and CD7 in T-cell lymphoma on a single slide. The utilization of fluorescent direct-labeled antibodies enables the triple staining of CD3, CD5, and CD7 without cross-reactivity, maintaining the same intensity as single stains. Moreover, we developed a joint Non-Negative Matrix Factorization-based Spatial Clustering Analysis (jNMF-SCA) with a modified spectral unmixing system, highlighting its potential as a supportive diagnostic tool for T-cell lymphoma.

Keywords: Spatial analysis, multiplex imaging, fluorescence imaging, computational biology, digital pathology, precision medicine, diagnostics

Introduction

Immunohistochemistry (IHC) using 3,3'-diaminobenzidine (DAB)[1, 2] serves as a foundational histochemical technique in routine pathology services for analyzing etiology and conducting histopathological diagnoses. Yet, the detection of multiple biomarkers proves challenging with conventional light microscopy. This challenge necessitates multiple serial tissue sections to ascertain the molecular and cellular locales of multiple biomarkers, significantly consuming tissue resources for examination. Furthermore, the application of serial sections complicates the analysis of identical cells in small cells, such as lymphocytes. Specifically, in the diagnosis of malignant T-cell lymphoma, especially in cases presenting scattered infiltrative types of lymphoma cells, the depletion of T-cell surface markers CD3, CD5, or CD7 in tissue specimens signals malignancy[3, 4]. However, confirming these biomarkers on the same cells for an accurate diagnosis presents difficulties with conventional IHC with DAB. While flow cytometry stands as the preferred diagnostic test, it is not universally accessible (Supplemental Table 1). The simultaneous detection of multiple antigens on histopathological sections has garnered interest not only for its research implications but also for its utility in predicting the response to anticancer drugs by examining the spatial arrangement of molecules and cells within the tissue microenvironment[5]. Recently, various multiplex fluorescent immunostaining methods have been reported, each reviewed for its distinctive characteristics[6].

The primary technique for identifying multiple biomarkers is fluorescence detection staining, which encompasses two principal categories. The first is a straightforward, direct single-step staining method that employs only the primary antibody[7 8]. The second approach involves multicolor staining and signal amplification through the sequential application of secondary antibodies, DNA oligos, enzymes, and other reactive molecules. The first category is represented by the direct method, while the second is represented by the indirect method[9], the cycle staining method[10, 11], the Tyramide Signal Amplification (TSA) method[12], and the oligo barcode method[13-15].

The direct method, known as the earliest approach to fluorescent immunostaining, relies on detecting the fluorescence intensity emitted by a dye attached to the antibody. However, its utility is limited by the challenge of distinguishing this fluorescence from the autofluorescence inherent in formalin-fixed paraffin-embedded (FFPE) tissue sections, a task complicated by the absence of signal amplification. As a result, the direct method has seen a decline in usage in contemporary practices. Conversely, the indirect method enhances the fluorescent signal through the use of a secondary antibody that binds to the primary antibody. However, this approach is limited by the specificity required in antibody combinations. The TSA method, while capable of signal amplification through the covalent accumulation of fluorescently labeled tyramide molecules on a tissue section via an enzymatic reaction, requires sequential antibody reactions. This process can obscure the

target antigen with previously accumulated fluorescently labeled tyramide molecules, complicating subsequent antigen-antibody reactions and the analysis of co-expression within the same cell[6]. Cycle staining methods and oligo barcode methods aim to address these limitations by binding staining molecules followed by their desorption. However, the repetitive nature of staining, imaging, and desorption processes can cause tissue distortion and damage, potentially leading to misalignment in overlapping imaging data[6].

Given these challenges, we were motivated to refine the multiple fluorescent immunostaining method through the application of spectral separation technology developed for flow cytometry[16] to tissue immunostaining. This methodological innovation is pivotal for obtaining spatial information through tissue immunostaining. Nonetheless, the emergence of wide-field imaging techniques, such as whole-slide imaging, complicates the identification of characteristic regions like the tissue microenvironment or scattered lymphoma cells. Existing methods that propose limiting the field of view to cells expressing specific biomarkers necessitate the establishment of thresholds, potentially introducing bias or overlooking significant regions[17]. To this effect, we developed a method that clusters samples based on the spatial distribution of cells in an unbiased manner across entire fields of view, enhancing our understanding of the tissue microenvironment and disease pathology beyond the capabilities of conventional methodologies.

Results

Spectral Imaging-based Single-Step Multiplex Immunofluorescence (SISS-mIF)

Here, we employ direct single-step staining for a straightforward and rapid execution of multiple fluorescent immunostaining. Multiple antibodies, each directly labeled with distinct fluorescent molecules, react in a singular step with an antigen on a tissue specimen (Fig. 1a). Fluorescence spectral data are gathered at a consistent speed for each excitation via a line scan, mirroring the process of a bright-field digital pathology slide scanner (Fig. 1b). The fluorescence spectrum data is compiled into a matrix, with the spectrum organized as rows and the spatial dimensions of x, y as columns. In direct single-step staining, differentiating labeled fluorescence from autofluorescence is critical, given the finite number of fluorescent molecules that can be conjugated with antibodies, and autofluorescence spectra derived as components from serial sections. Unmixed images are procured by segregating the spectral data matrix, collected from the immunostained section, using the least squares method (LSM) with both optimized autofluorescence spectra from the spectral data matrix derived from the non-immunostained serial section through non-negative matrix factorization (NMF)[18-21] and the spectra of the fluorescence tagged to the antibodies (Fig. 1c). Each pixel in the image is denoted as antibodies/voxel, enabling an evaluation that is independent of the labeled fluorescent molecular species (Fig. 1d).

Hyperspectral Imaging

Spectrum cube data was obtained by a Line-scan spectrum imaging system, assembled from a commercially available microscope with a x20 objective lens. An emitted laser is shaped into a flat-top beam profile using a cylindrical lens array, a scanning mirror to negate any interference pattern, and a custom-made monochromator (Fig. 2a). An Offner-type monochromator was selected for imaging spectroscopy, casting spatial and wavelength axes in two dimensions on an image sensor in a single exposure with a custom grating (Fig. 2b). Scans were conducted with each of the 4-excitation lasers. Unlike conventional fluorescence imaging, where a fluorescence filter is designated for each fluorescent molecule, this system minimized the effect of photobleaching due to uniform exposure time control across all fluorescent molecules, notwithstanding the disparate exposure times necessitated by repeated exposure and illumination for each fluorescent molecule.

Spectral Unmixing

The spectral unmixing process benefits from the acquisition of autofluorescence spectra, characterized by the separation into autofluorescence components and optimization of each component's spectrum from actual sample data. The autofluorescence spectra from different cells vary based on the contained autofluorescence molecules[22] and are also influenced by tissue fixation conditions[23, 24]. The separation of autofluorescence spectrum components aligns with cellular type differences and is optimized from spectral data acquired from unstained slides, starting with five fluorescence spectra: NADH and FAD as fluorescent nucleotides, arachidonic acid for lipids, porphyrins constituting hemoglobin and cytochrome, and the mounting agent (Fig. 3a). Each component spectrum's optimization is executed via NMF, ensuring each spectrum is refined under conditions that preclude negative values to minimize residuals across all pixel spectral data[25, 26] (Fig. 3b). With both the optimized autofluorescence spectra and the fluorescent antibody spectra at hand, unmixing of the original spectrum cube is performed by LSM[16]. The reference spectra for fluorescent antibodies are ascertained by slide samples wherein they are dispersed to a known concentration and normalized from the sensor surface volume as the concentration with one molecule present per unit voxel. These normalized reference spectra are fed into the LSM, outputting an image displaying the number of molecules per voxel in each pixel (Fig. 3c).

Direct Single-Step Staining Multiplex Immunofluorescence

Direct single-step staining for multiplex immunofluorescence was prepared with three panels of fluorescently labeled antibodies. The first panel, designed for tonsil specimens, included Alexa Fluor (AF)488-CD4, AF555-PD-1, AF568-ki67, AF647-PDL1, AF680-CD3, AF700-Cytokeratin, AF750-CD8, and AF790-CD68, the second panel for

skin comprised AF488-CD45RO, AF555-CD3, AF647-PD-1, AF680-Sox10, and AF750-Cytokeratin, and the third panel for breast contained AF488-CD4, eF570-Foxp3, eF615-CD20, AF647-CD8, AF680-CD68, and AF750-Cytokeratin, all showing specific staining without background interference for the majority of the markers (Fig. 4a-c). Since CD3, CD4, CD8, CD20, CD45RO, PD-1, and PD-L1 exhibited staining on the cell membrane, ki67, Foxp3, and Sox10 demonstrated nuclear staining, and Cytokeratin and CD68 highlighted the cytoplasm, the determination of specific staining was based on the observed staining morphology and localization.

Image Output in Antibody Count

In the evaluation of antibody count as an image output, if the number of antibodies is computed through normalization using the reference spectrum, this calculated antibody count should remain consistent regardless of variations in imaging conditions. To test this methodology, images of slides stained under identical conditions from serial sections of a human tonsil tissue FFPE block were captured under varying scan conditions (Fig. 5a), and the resultant antibody counts were juxtaposed (Fig. 5b). Comparable values were observed for all antibodies, AF488-αCD7, AF555-αCD3, and AF647-αCD5, under three different scan conditions: the first with standard settings, the second where the exposure time was halved, and the third where both the exposure time and the gain were reduced by half. In exploring the potential for co-expression analysis on the same cell, the antibody counts following single, duplex, and triplex staining with α-CD3, α-CD3 & α-CD5, and α-CD3, α-CD5, and α-CD7 respectively on serial sections of human tonsil tissue were compared (Fig. 5c). The percentage of α-CD3 antibody in both duplex and triplex staining configurations was 97 ± 16% and 92 ± 10%, respectively, assuming the count in simplex staining as 100%. These findings indicate equivalent antibody presence across all staining modalities.

Detection of CD3, CD5, and CD7 from the Single Section in T-cell Lymphoma

The efficacy of detecting CD3, CD5, and CD7 from a single section in T-cell lymphoma was evaluated by comparing the expression levels of each marker using DAB-IHC (IHC) and multiplex immunofluorescence (mIF) against their counterparts measured by flow cytometry (FCM). Instances of weak expression (e.g., FCM dim+, IHC weakly+) or absence detected by FCM, DAB-IHC, or mIF were deemed negative. Representative images of IHC and mIF staining were presented (Fig. 6 a-c), and a comparison of FCM, IHC, and mIF results was tabulated (supplemental Table 2). An evaluation of all CD3, CD5, and CD7 expressions showed a concordance rate with FCM of 21 cases (84.0%) and 4 cases (16.0%) of discordance when utilizing mIF. Conversely, IHC indicated 18 cases (72.0%) of concordance and 7 cases (28.0%) of discordance. Among the six cases with CD5 deletions, mIF demonstrated a concordance in 5 cases (83.3%) and discordance in 1

case (16.7%), whereas IHC presented a 50-50 split with 3 cases concordant and 3 cases discordant. Similarly, in evaluating 18 patients with CD7 deletions, mIF achieved a concordance in 16 cases (88.9%) and discordance in 2 cases (11.1%), compared to IHC which showed 14 cases (77.8%) of concordance and 4 cases (22.2%) of discordance. Hence, mIF outperformed IHC across all metrics. For cases with discrepancies, mIF tended to be marginally more sensitive, with IHC-negative cases more likely to test positive with mIF (Table 1).

CD3 staining in a target-like pattern inside the CD5 or CD7 membrane-positive images was observed, allowing visualization of cytoplasmic-CD3 (Fig. 6d). This finding was similar to the CD3 ζ intracytoplasmic expression picture in TCRα mutant T cells and was consistent with cytoplasmic-CD3 staining[27]. Of the 16 cases showing cytoplasmic-CD3 in FCM, the above staining image was also confirmed in 14 cases (87.5%) in mIF (Table 1).

jNMF-Based Spatial Clustering Analysis (jNMF-SCA)

The joint Non-Negative Matrix Factorization based Spatial Clustering Analysis (jNMF-SCA) was developed to categorize case samples and highlight characteristic regions within each classification to aid pathologists in phenotyping. jNMF, an algorithm for dimension reduction and feature extraction in multiplex analysis using multiple samples, facilitates multimodal analysis encompassing multidimensional data such as gene expression[28–30]. By decomposing multiple matrices into a common basis matrix W and feature values H, jNMF simplifies data complexity and reduces dimensionality, allowing the correlation pattern between multiple elements to be elucidated by projecting multiple matrices into a new shared space (Fig. 7a). To cluster samples by the spatial distribution of various phenotypic cells and to extract their characteristic regions using jNMF, whole slide images were segmented into subregions of $300 \times 300\ \mu m^2$, with the number of biomarker-positive cells quantified for each subregion. This study aimed to identify samples and regions containing cells with deletions of CD5 or CD7 in CD3-positive T-cell lymphoma. Subregions were organized by the total count of CD3 positive (+) cells, generating a matrix for the percentage of CD5 negative (-) cells or CD7 negative (-) cells, respectively, arranged as columns of sorted subregions and rows of samples (Fig. 7b). Subregions with a higher number of CD3(+) T cells were sequentially positioned from left to right in the matrix column. This ordering facilitated the interpretation of marker correlation, as the expression of CD3, CD5, and CD7 on normal T cells is correlated. Sorting the subregion space in descending order of CD3(+) cells highlighted the correlation among markers more straightforwardly.

Through the preprocessing steps mentioned, jNMF compresses the data's dimensionality by decomposing several sample matrices into a common basis matrix W

for clustering samples and a feature value H characterized by the distribution of multiple cell types (Fig. 7c). To illustrate the analysis results, X1 represents a matrix of the CD5(-) cell ratio sorted in descending order of the number of CD3(+) cells in each subregion, and X2 is a matrix of the CD7(-) cell ratio sorted similarly. The first column of W corresponds to Cluster 1 (CL1), indicating samples with high values of CD5(-) or CD7(-) cells in certain regions, and the second column corresponds to Cluster 2 (CL2). The feature vectors H for each cluster—CL1 and CL2—identify the regions with significant contributions for each cluster. The common factor matrix W aids in observing cluster classification, while the feature matrix H extracts regions with a high density of CD5(-) or CD7(-) cells, indicated by the orange and blue areas in the H matrix for CL1 and CL2, respectively (Fig. 7c).

Assisted Diagnosis of T-cell Lymphoma Using jNMF-SCA

For the assisted diagnosis of T-cell lymphoma using jNMF-SCA, a total of 30 case samples, including 14 control samples and 16 T-cell lymphomas, were grouped into 2 clusters. Control samples were associated with low z-score assignments to either cluster, while T-cell lymphoma samples exhibited high z-score assignments to one or both clusters, as depicted in the W matrix. Cluster 1 (CL1) was characterized by CD5 deletions in regions with relatively few CD3(+) cells, as shown by H1, and CD7 deletions in regions with low to medium CD3(+) cell counts, as indicated by H2. Conversely, Cluster 2 (CL2) encompassed regions with consistent CD5 expression, as shown by H1, and a broad range of regions with CD7 deletions, as depicted by H2 (Fig. 8a).

To retrospectively detect samples suspected of harboring CD5 or CD7 negative T-cell lymphoma, a criterion was established defining such samples as those with a z-score in CL1 or CL2 of the W matrix exceeding the mean plus three times the standard deviation ($\mu+3\sigma$) of the control sample. This result was then compared to the subjective evaluation by the pathologist, who considered both dim detection and partial region negative detection as negative (Supplemental Table 3). Out of the total 30 samples, including controls, 16 were identified by the pathologist as having CD5 or CD7 deletions, 15 of which were also detected as such by jNMF (true positives, TP). Furthermore, 14 specimens were deemed by the pathologist as triple positive, with 12 of these also classified as triple positive by jNMF (true negatives, TN). The analysis yielded a sensitivity of 93.75%, a specificity of 85.71%, and an overall correct response rate of 90.00% (Table 2). These outcomes demonstrate jNMF's high sensitivity in detecting regions of deletion, including those considered dim or only affecting specific regions.

The pathologist's phenotypic determinations were guided by the jNMF-SCA result display. For instance, Case sample 24 was assessed as CD3(+), CD5(+), CD7(-) by both the pathologists and jNMF. Focusing on the area with a high CD7(-) ratio as presented by jNMF-SCA facilitated the pathologist's identification of the CD7 deletion area, which was not extensive across the entire field of view (highlighted by the white box in Fig. 8b). In

the targeted field of view, this sample contained CD3-cytoplasmic positive cells that did not merge with either CD5 or CD7, but co-expression of CD5 was confirmed in the same cells, while numerous CD7 deletion cells were observed (Fig. 8b).

Discussion

By developing spectral imaging acquisition and spectral separation technologies that differentiate fluorescent signals from autofluorescent signals, we have facilitated multiple fluorescence imaging via the direct method. This approach allows for the simultaneous imaging of up to nine types of fluorescent markers, including 8 colors plus 4',6-Diamidine-2'-phenylindole dihydrochloride (DAPI). The technology streamlines and accelerates data acquisition by enabling staining and scanning in a single step each, simplifying the operational process—a crucial improvement for diagnostic workflows. For instance, unlike cycle staining and scanning, which, even when automated, monopolize the equipment for extended periods, our method enhances throughput in diagnostics and laboratory workflows involving numerous specimens.

Moreover, akin to the capabilities of a flow-cytometer, our method's multiplicity expands with the availability of primary antibodies tagged with fluorescent dyes, allowing staining and scanning in one step without complicating the operational process from start to finish or necessitating staining order consideration. Conversely, TSA and cyclic staining methods require additional steps for staining or imaging as the number of fluorescent colors increases, necessitating the optimization of staining order. This not only lengthens the time needed for assay optimization and the entire assay process but also risks damaging the tissue section due to repeated solution reactions, potentially resulting in the loss of valuable specimens through peeling and defects. While similar one-step immunostaining has been proposed using microscope systems with bandpass fluorescence filters, limitations exist on the fluorophores that can be utilized to match the filter's wavelength[31]. Our method, utilizing hyperspectral spectroscopy, NMF, and LSM, offers a broader selection of fluorophores thanks to its superior spectral separation capabilities. A notable challenge with one-step immunostaining is ensuring consistent antigen activation conditions, as some antibody clones necessitate specific activation conditions, like enzymatic reactions. Nevertheless, many immunostainings commonly perform antigen activation under uniform conditions, akin to mass spectrometric tissue imaging. Consequently, SISS-mIF, capable of completing staining and imaging in a singular process, is optimally suited for diagnostic and laboratory workflows.

Our technique, which outputs images based on antibody counts rather than fluorescent intensity, has demonstrated the capability to display images within a similar dynamic range, irrespective of image capture conditions or multiplex staining (Fig. 5). This method is particularly effective when combined with our spectral unmixing technique; otherwise, incomplete spectral unmixing, including autofluorescence, may lead to

inaccurate antibody counts. Anticipated to diminish batch effects in case sample analyses, this technique has indeed standardized data processing across all T-cell lymphoma case samples, regardless of acquisition times, including setting thresholds for marker expression.

The SISS-mIF holds promise for aiding lymphoma diagnosis. It enables precise co-expression evaluation of CD3, CD5, and CD7 within the same cell and facilitates accurate identification of biomarker expression locations, distinguishing between cell membrane and cytoplasm expressions (Fig. 6d). Moreover, it allows for the detection of regions with CD5 and CD7 expression deficiencies, offering analysis beyond phenotype distribution, akin to flow cytometry, by incorporating region information and potentially linking to malignant areas, such as those characterized by nuclear dysplasia. Overall, mIF proved superior to IHC in all results, with a trend of IHC-negative cases being positive in mIF (Fig. 6). To enhance these outcomes, exploring cut-off values through antibody count quantification or adjusting each antibody with control samples may prove beneficial.

Additionally, our jNMF-SCA could notably support lymphoma diagnosis. Although high sensitivity is desirable, the analysis included one false negative (Table 2). Case sample 26, classified as a false negative, presented a challenging scenario as determined by the pathologist, exhibiting both full and partial positive expressions across CD3, CD5, and CD7. Notably, this sample exhibited higher antibody counts for CD3, CD5, and CD7 than other case samples, falling below jNMF's detection threshold using a common threshold (Supplemental Fig. 3).

Opting not to use jNMF-SCA for phenotype determination and instead employing its display output to guide the pathologist has also proven effective (Fig. 8b). This guidance functionality can efficiently and accurately pinpoint lesions, proving valuable for pathological evaluations, even in scenarios where a minimal number of lymphoma cells infiltrate the epidermis or adipose tissue in skin samples. Heatmaps generated by jNMF-SCA elucidate the negative rates of CD5 and CD7 in subregions, arranged in descending order of CD3 presence. Subregions towards the right tend to exhibit higher negative rates due to their peripheral tissue location, which naturally contains fewer T cells, leading to increased missing rates upon detecting autofluorescence (Fig. 8b CD5). While there remains room for enhancement in data preprocessing for jNMF-SCA input and result output display, this methodology is anticipated to extend beyond T-cell lymphoma diagnosis assistance to other lymphomas and quantitative tumor microenvironment evaluation. Although synergizing with SISS-mIF improves positive/negative marker expression determination, jNMF-SCA could also complement other multiplex imaging methodologies. This adaptability allows jNMF-SCA not just to be paired with immunofluorescence but also to be applicable to hyperplex imaging, including spatial transcriptomics. Further studies are necessary to explore these applications[32-34].

In summary, the combination of SISS-mIF and jNMF-SCA offers a robust framework for enhancing diagnostic accuracy and efficiency in lymphoma and potentially

other cancers. SISS-mIF's ability to accurately evaluate co-expression and precisely identify biomarker expression locations, coupled with jNMF-SCA's high sensitivity and guidance functionality, presents a significant advancement in diagnostic methodologies. The utilization of heatmaps to display subregion-specific negative rates of CD5 and CD7 further aids in the nuanced analysis of lymphoma, allowing for a more detailed examination of the tumor microenvironment. While both SISS-mIF and jNMF-SCA show great promise individually, their combined use could revolutionize the approach to lymphoma diagnosis, providing pathologists with a powerful toolset for identifying and characterizing disease with unprecedented precision.

Methods

Tissue Slides

For the purposes of multiplex immunofluorescent staining, we utilized human tonsil tissue, human skin tissue, and human breast tissues, which were diagnosed as reactive follicular hyperplasia, nodular melanoma, and infiltrating ductal carcinoma, respectively. These tissue specimens were acquired from BioIVT, LLC (Westbury, NY)., with informed consent obtained from the source, excluding personal information. For the T-cell lymphoma study, twenty-five formalin-fixed, paraffin-embedded (FFPE) specimens from T-cell lymphoma patients at Tokyo Medical and Dental University Hospital (Tokyo, Japan), spanning from 2014 to 2021 with accompanying flow cytometry data, were examined. Control samples comprised 10 non-neoplastic lymph node specimens and 3 inflamed skin specimens from the same institution. This study received approval from the institutional ethics board (M2019-204). All tissues were sectioned at 4-μm thickness and placed on CREST slide glass (Matsunami Glass Ind., Ltd., Osaka, Japan).

Immunostaining

IF and IHC assays were conducted using a fully automated stainer, BOND RXm (Leica Biosystems, Nussloch, Germany), according to the manufacturer’s guidelines. Slides underwent de-paraffinization with Bond Dewax Solution (Leica Biosystems) for 30 min at 60 °C. Epitope retrieval was performed using BOND Epitope Retrieval Solution 2 (Leica Biosystems) for 20 min at 100 °C. Primary antibodies, as listed in Supplemental Table 4, were diluted with BOND Primary Antibody Dilution (Leica Biosystems) to a specific concentration and applied to the slides, which were then incubated at room temperature for 30 min. For brightfield detection, slides were stained with DAB and hematoxylin utilizing BOND Polymer Refine Detection (Leica Biosystems) as per the manufacturer's instructions, followed by dehydration, permeabilization, and mounting with Pathomount (FUJIFILM Wako Pure Chemical Corp., Osaka, Japan) and a cover glass. For fluorescent detection, slides underwent antibody incubation followed by DAPI staining and

were mounted with ProLong Diamond Antifade Mountant (Thermo Fisher SCIENTIFIC, Waltham, Massachusetts,) and a cover glass.

Hyperspectral Imaging

The line-scan spectrum imaging system was assembled from a commercially available BX63 microscope (Olympus, Tokyo, Japan) with a x20 objective lens, a laser light source, and a custom-made monochromator. Four lasers were utilized for excitation (405 nm: NDV7116(Nichia corp., Tokushima, Japan), 488 nm: NDS7175E (Nichia corp.), 532 nm: VFL-P-1000-532-OEM1-B1(MPB Communications Inc.), 638 nm: HL63193MG (Ushio Inc., Tokyo, Japan). The wavelength resolution of the Offner-type monochromator was set at 8 nm. A CMOS camera captured the spectrum image. An excitation filter was selected for each laser (ZET405/20x, ZET488/10x, ZET532/10x, ZET642/20x (Chroma Technology corp., Bellows Falls, VT). Dichroic mirrors and emission filters were chosen with a 4-band filter respectively (ZT405/488/532/640rpc-XT, ZET405/488/532/642m (Chroma Technology corp.).

Image Shading Correction

Shading correction was conducted by deriving the shading pattern from all spectral cubes acquired by the system and incorporating the reciprocal values into each spectral cube. Following shading correction, spectral unmixing was performed on the corrected spectrum cube using the reference spectrum.

Image Deconvolution

A 1-μm pinhole light source with a defined structure was imaged using a line-scan spectral imaging system to capture its intensity distribution. The device's intrinsic point spread function was identified by fitting the ideal intensity distribution of a 1-μm aperture into the actual intensity distribution captured by the device. Subsequently, the image underwent processing with Richardson-Lucy deconvolution[35, 36], using the derived point spread function.

Image Stitching

Unmixing occurred for each default size (2432 × 640 pix), and stitching was employed for a comprehensive field of view. Each default size data included a gloss of approximately 5% (128 pix) per side, and deviations in the x and y directions were calculated by template matching within that region[37]. A wide-field image was compiled by accounting for these deviations and performing stitching.

Image Cytometry Analysis

Stitched images were segmented into small regions (blocks) of 300 × 300 μm^2. Following cell segmentation and expansion treatments, the number of antibodies per cell for biomarkers (CD3, CD5, and CD7) was calculated. Cell segmentation utilized nuclear detection algorithm based on DAPI signal, and the expansion process extended 4 pixels from the nucleus. The antibody count per cell was ascertained by averaging pixels corresponding to the expanded area. Cells exceeding the antibody number threshold for each biomarker were identified as positive cells. The threshold for determining positive cells for each biomarker was set at the 98th percentile of antibody numbers per DAPI-positive cell in the unmixed images assigned to each marker in non-immunostained images of control samples. This approach to determining positive cells by antibody counts, set at thresholds for each marker, resulted in more than 85% of CD3 positive cells being concurrently positive for CD3, CD5, and CD7 in immunostained images of all control samples, underscoring the method's precision.

Data Imputation for jNMF-SCA

To construct the matrix for jNMF-SCA, aligning the number of rows (i.e., the number of subregions) is essential. jNMF's effectiveness in clustering can be influenced when more than 10% of the data is completed with zeros[29]. In this study, the number of subregions for all case samples was standardized to 110, the maximum value among the samples, for all 30 case samples. The imputed row data were augmented by randomly extracting subregions until reaching a total of 110, ensuring uniformity across samples.

Extracting Cluster Membership After jNMF-SCA

Following jNMF, the resulting matrix W was standardized using Z-scores to facilitate comparison and analysis. The Z-scores of matrix W were calculated using the following equation:

$$Z_{ij} = \frac{w_{ij} - \mu}{\sigma}$$

where μ represents the mean value of W, and σ represents the standard deviation of W. This standardization allowed for the evaluation of cluster membership based on statistical significance. The population of Z-scores for control samples (Sample #1~Sample #9) for each cluster was estimated using the maximum likelihood method, from which the mean value μ and standard deviation σ of the estimated population were determined. A cutoff value of μ+3σ was then set for each cluster, with samples exceeding this value classified within clusters and considered as negative judgments in jNMF, enhancing the method's specificity in cluster determination.

Phenotyping by Pathologist

Phenotype determination using fluorescence imaging was performed by three pathologists employing an in-house image viewer, setting the threshold for each marker at the 99.8th percentile of the antibody count per cell in the fluorescent images, excluding autofluorescence components. Two rounds of evaluation were performed, leveraging the guidance function of jNMF-SCA. Discrepancies between the first and second round evaluations prompted a discussion among the pathologists, culminating in a consensus decision. In comparing results with jNMF, evaluations by the pathologists were aggregated as negative even if detected partially negative or classified as dim, aiming for a conservative and accurate diagnostic approach. This methodological rigor ensures a high level of precision in lymphoma diagnosis, facilitating effective treatment planning and patient care.

References

1. Nakane, P.K. & Pierce, G.B., Jr. Enzyme-labeled antibodies: preparation and application for the localization of antigens. J. Histochem. Cytochem. 14, 929-931 (1966).
2. Sternberger, L.A., Hardy, P.H., Jr., Cuculis, J.J. & Meyer, H.G. The unlabeled antibody enzyme method of immunohistochemistry: preparation and properties of soluble antigen-antibody complex (horseradish peroxidase-antihorseradish peroxidase) and its use in identification of spirochetes. J. Histochem. Cytochem. 18, 315-333 (1970).
3. Zain, J.M. & Hanona, P. Aggressive T-cell lymphomas: 2021 Updates on diagnosis, risk stratification and management. Am. J. Hematol. 96, 1027-1046 (2021).
4. Zhang, X., Zhou, J., Han, X., Wang, E. & Zhang, L. Update on the Classification of and Diagnostic Approaches to Mature T-Cell Lymphomas. Arch. Pathol. Lab. Med. 146, 947-952 (2022).
5. Lu, S. et al. Comparison of Biomarker Modalities for Predicting Response to PD-1/PD-L1 Checkpoint Blockade: A Systematic Review and Meta-analysis. JAMA Oncol 5, 1195-1204 (2019).
6. Taube, J.M. et al. The Society for Immunotherapy of Cancer statement on best practices for multiplex immunohistochemistry (IHC) and immunofluorescence (IF) staining and validation. J Immunother Cancer 8 (2020).
7. Berliner, A.H.C.H.J.C.R.N.J.E. The Demonstration of Pneumococcal Antigen in Tissues by the Use of Fluorescent Antibody. J. Immunol. 45, 159-170 (1942).
8. Coons, A.H. & Kaplan, M.H. Localization of antigen in tissue cells; improvements in a method for the detection of antigen by means of fluorescent antibody. J. Exp. Med. 91, 1-13 (1950).
9. Wang, B.L. & Larsson, L.I. Simultaneous demonstration of multiple antigens by indirect immunofluorescence or immunogold staining. Novel light and electron

microscopical double and triple staining method employing primary antibodies from the same species. Histochemistry 83, 47-56 (1985).

10. Gerdes, M.J. et al. Highly multiplexed single-cell analysis of formalin-fixed, paraffin-embedded cancer tissue. Proc. Natl. Acad. Sci. U. S. A. 110, 11982-11987 (2013).
11. Lin, J.R., Fallahi-Sichani, M. & Sorger, P.K. Highly multiplexed imaging of single cells using a high-throughput cyclic immunofluorescence method. Nat Commun 6, 8390 (2015).
12. Stack, E.C., Wang, C., Roman, K.A. & Hoyt, C.C. Multiplexed immunohistochemistry, imaging, and quantitation: a review, with an assessment of Tyramide signal amplification, multispectral imaging and multiplex analysis. Methods 70, 46-58 (2014).
13. Goltsev, Y. et al. Deep Profiling of Mouse Splenic Architecture with CODEX Multiplexed Imaging. Cell 174, 968-981 e915 (2018).
14. Phillips, D. et al. Immune cell topography predicts response to PD-1 blockade in cutaneous T cell lymphoma. Nat Commun 12, 6726 (2021).
15. Wharton, K.A., Jr. et al. Tissue Multiplex Analyte Detection in Anatomic Pathology - Pathways to Clinical Implementation. Front Mol Biosci 8, 672531 (2021).
16. Futamura, K. et al. Novel full-spectral flow cytometry with multiple spectrally-adjacent fluorescent proteins and fluorochromes and visualization of in vivo cellular movement. Cytometry A 87, 830-842 (2015).
17. Berry, S. et al. Analysis of multispectral imaging with the AstroPath platform informs efficacy of PD-1 blockade. Science 372 (2021).
18. Pentti Paatero, U.T. Positive matrix factorization: A non-negative factor model with optimal utilization of error estimates of data values. Environmetrics 5, 111-126 (1994).
19. Lee, D.D. & Seung, H.S. Learning the parts of objects by non-negative matrix factorization. Nature 401, 788-791 (1999).
20. Mitsufuji, S.U.F.G.Y. Deep neural network based instrument extraction from music. 2015 IEEE International Conference on Acoustics, Speech and Signal Processing (ICASSP), 2135-2139 (2015).
21. Stefan Uhlich, M.P., Franck Giron, Michael Enenkl, Thomas Kemp,Naoya Takahashi and Yuki Mitsufuji Improving music source separation based on deep neural networks through data augmentation and network blending. 2017 IEEE International Conference on Acoustics, Speech and Signal Processing (ICASSP), 261-265 (2017).
22. Croce, A.C. & Bottiroli, G. Autofluorescence spectroscopy and imaging: a tool for biomedical research and diagnosis. Eur. J. Histochem. 58, 2461 (2014).

23. Majumder, S.K., Ghosh, N. & Gupta, P.K. N2 laser excited autofluorescence spectroscopy of formalin-fixed human breast tissue. J. Photochem. Photobiol. B 81, 33-42 (2005).
24. Siddaramaiah, M. et al. Identification of protein secondary structures by laser induced autofluorescence: A study of urea and GnHCl induced protein denaturation. Spectrochim. Acta. A Mol. Biomol. Spectrosc. 174, 44-53 (2017).
25. Ortega-Martorell, S., Lisboa, P.J., Vellido, A., Julia-Sape, M. & Arus, C. Non-negative matrix factorisation methods for the spectral decomposition of MRS data from human brain tumours. BMC Bioinformatics 13, 38 (2012).
26. Jimenez-Sanchez, D., Ariz, M., Morgado, J.M., Cortes-Dominguez, I. & Ortiz-de-Solorzano, C. NMF-RI: blind spectral unmixing of highly mixed multispectral flow and image cytometry data. Bioinformatics 36, 1590-1598 (2020).
27. Brazin, K.N. et al. The T Cell Antigen Receptor alpha Transmembrane Domain Coordinates Triggering through Regulation of Bilayer Immersion and CD3 Subunit Associations. Immunity 49, 829-841 e826 (2018).
28. Yang, Z. & Michailidis, G. A non-negative matrix factorization method for detecting modules in heterogeneous omics multi-modal data. Bioinformatics 32, 1-8 (2016).
29. Fujita, N., Mizuarai, S., Murakami, K. & Nakai, K. Biomarker discovery by integrated joint non-negative matrix factorization and pathway signature analyses. Sci. Rep. 8, 9743 (2018).
30. Shiga, M., Seno, S., Onizuka, M. & Matsuda, H. SC-JNMF: single-cell clustering integrating multiple quantification methods based on joint non-negative matrix factorization. PeerJ 9, e12087 (2021).
31. Lin, J.R. et al. High-plex immunofluorescence imaging and traditional histology of the same tissue section for discovering image-based biomarkers. Nat Cancer 4, 1036-1052 (2023).
32. Giesen, C. et al. Highly multiplexed imaging of tumor tissues with subcellular resolution by mass cytometry. Nat Methods 11, 417-422 (2014).
33. Stahl, P.L. et al. Visualization and analysis of gene expression in tissue sections by spatial transcriptomics. Science 353, 78-82 (2016).
34. He, S. et al. High-plex imaging of RNA and proteins at subcellular resolution in fixed tissue by spatial molecular imaging. Nat. Biotechnol. 40, 1794-1806 (2022).
35. Hanisch, R.J., White, R.L. & Gilliland, R.L. Deconvolution of Hubbles Space Telescope images and spectra. (1996).
36. Biggs, D.S. & Andrews, M. Acceleration of iterative image restoration algorithms. Appl Opt 36, 1766-1775 (1997).
37. Brunelli, R. Template Matching Techniques in Computer Vision: Theory and Practice. (Wiley, 2009).

Figures

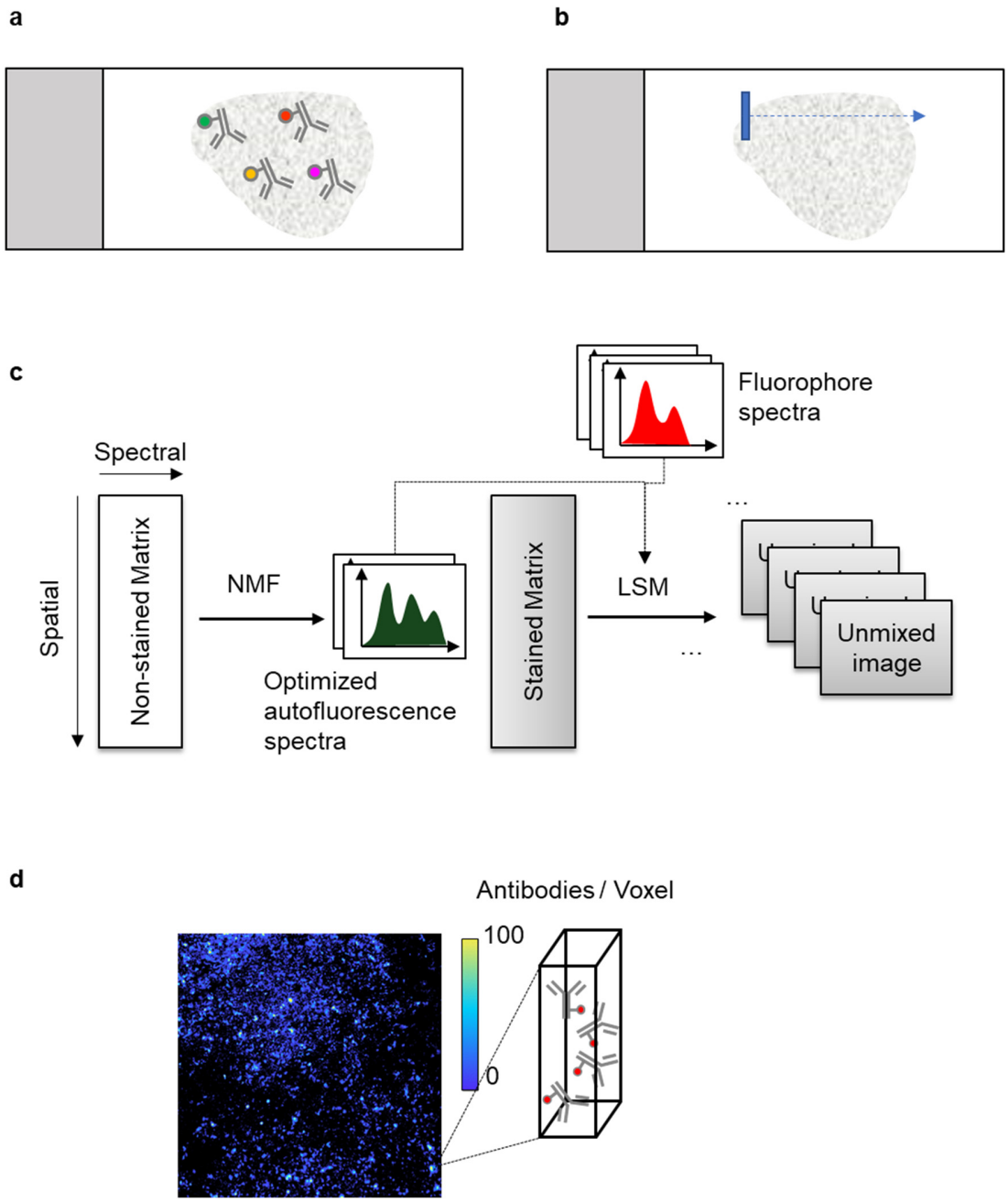

Figure 1.

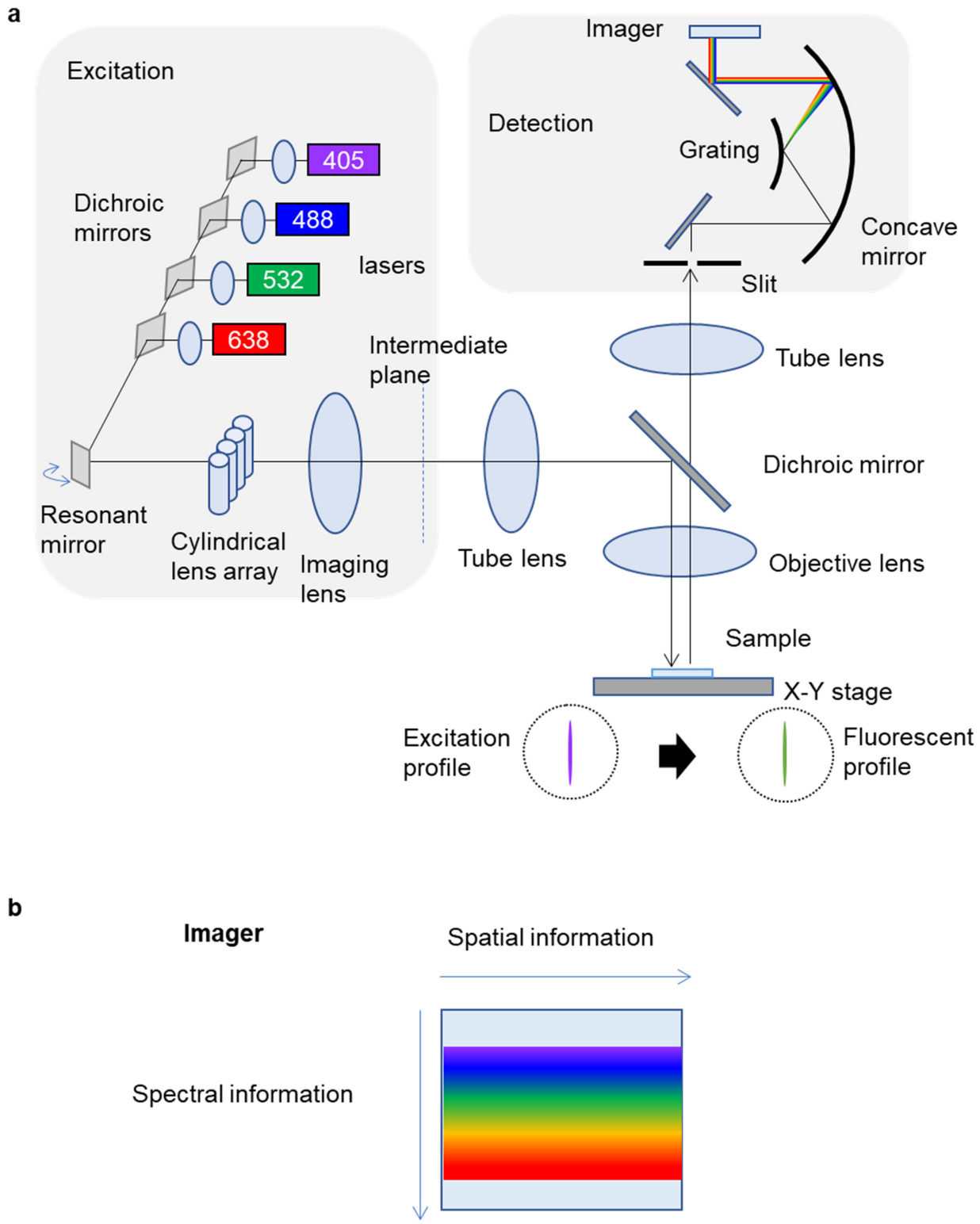
a
Excitation
Imager
Detection
Grating
Concave mirror
Slit
405
488
532
638
Dichroic mirrors
lasers
Intermediate plane
Tube lens
Dichroic mirror
Resonant mirror
Cylindrical lens array
Imaging lens
Tube lens
Objective lens
Sample
X-Y stage
Excitation profile
Fluorescent profile
b
Imager
Spatial information
Spectral information

Figure 2.

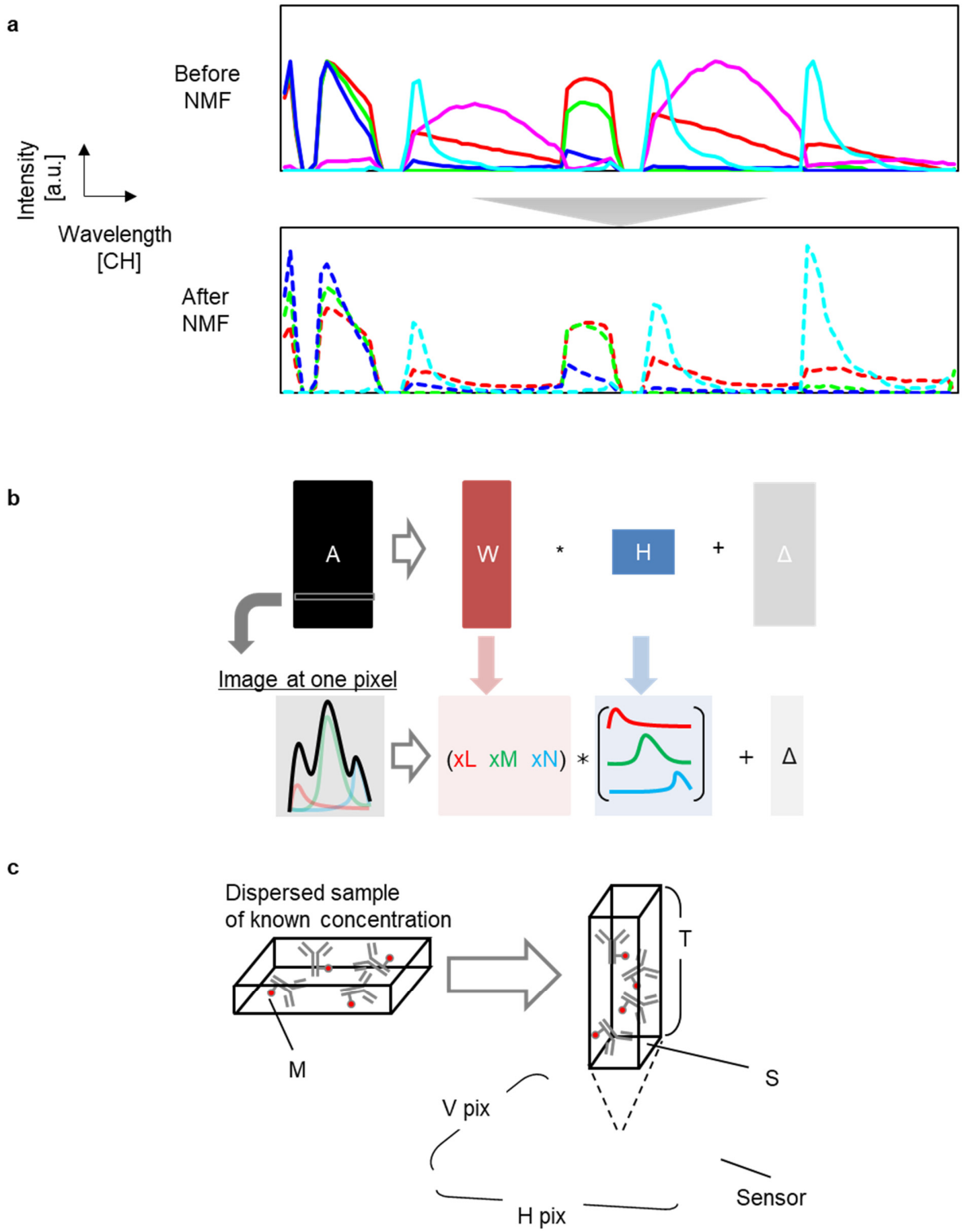
a
Before NMF
Intensity [a.u.]
Wavelength [CH]
After NMF
b
A
W
*
H
+
Δ
Image at one pixel
(xL xM xN) *
+ Δ
c
Dispersed sample of known concentration
M
T
S
V pix
H pix
Sensor

Figure 3.

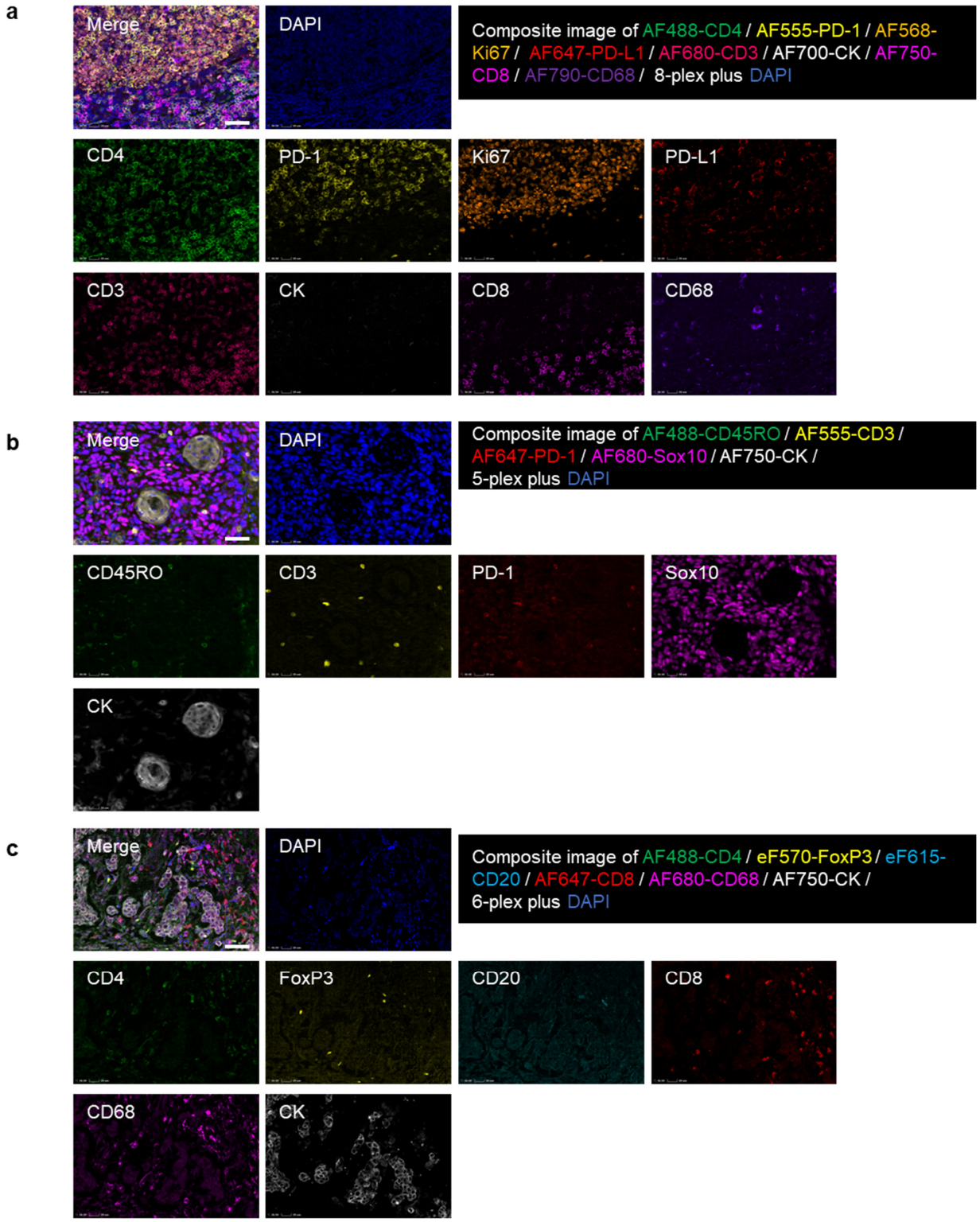
a
Merge
DAPI
Composite image of AF488-CD4 / AF555-PD-1 / AF568-Ki67 / AF647-PD-L1 / AF680-CD3 / AF700-CK / AF750-CD8 / AF790-CD68 / 8-plex plus DAPI
CD4
PD-1
Ki67
PD-L1
CD3
CK
CD8
CD68
b
Merge
DAPI
Composite image of AF488-CD45RO / AF555-CD3 / AF647-PD-1 / AF680-Sox10 / AF750-CK / 5-plex plus DAPI
CD45RO
CD3
PD-1
Sox10
CK
c
Merge
DAPI
Composite image of AF488-CD4 / eF570-FoxP3 / eF615-CD20 / AF647-CD8 / AF680-CD68 / AF750-CK / 6-plex plus DAPI
CD4
FoxP3
CD20
CD8
CD68
CK

Figure 4.

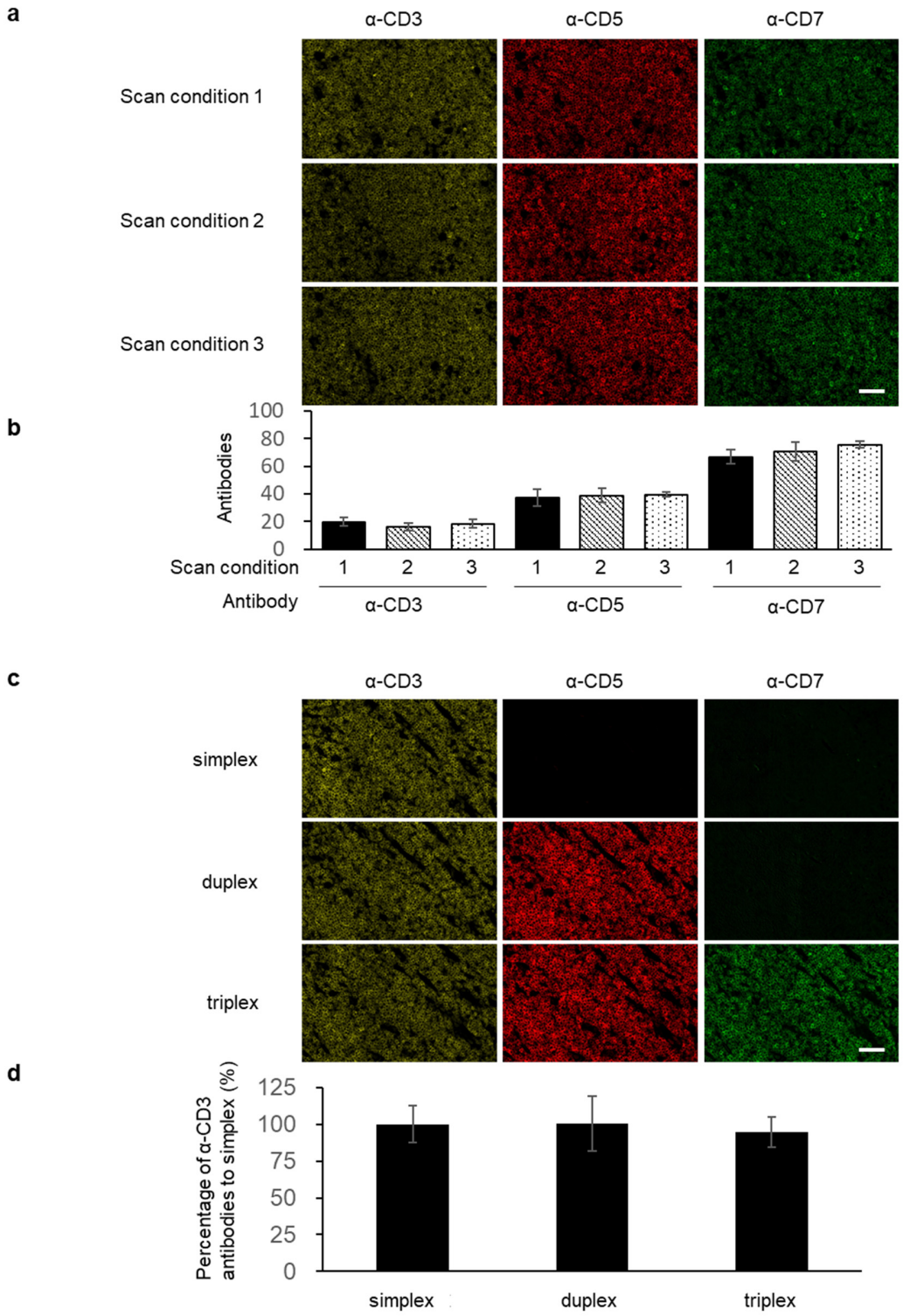
a
α-CD3
α-CD5
α-CD7
Scan condition 1
Scan condition 2
Scan condition 3
b
Antibodies
100
80
60
40
20
0
Scan condition
1
2
3
1
2
3
1
2
3
Antibody
α-CD3
α-CD5
α-CD7
c
α-CD3
α-CD5
α-CD7
simplex
duplex
triplex
d
Percentage of α-CD3 antibodies to simplex (%)
125
100
75
50
25
0
simplex
duplex
triplex

Figure 5.

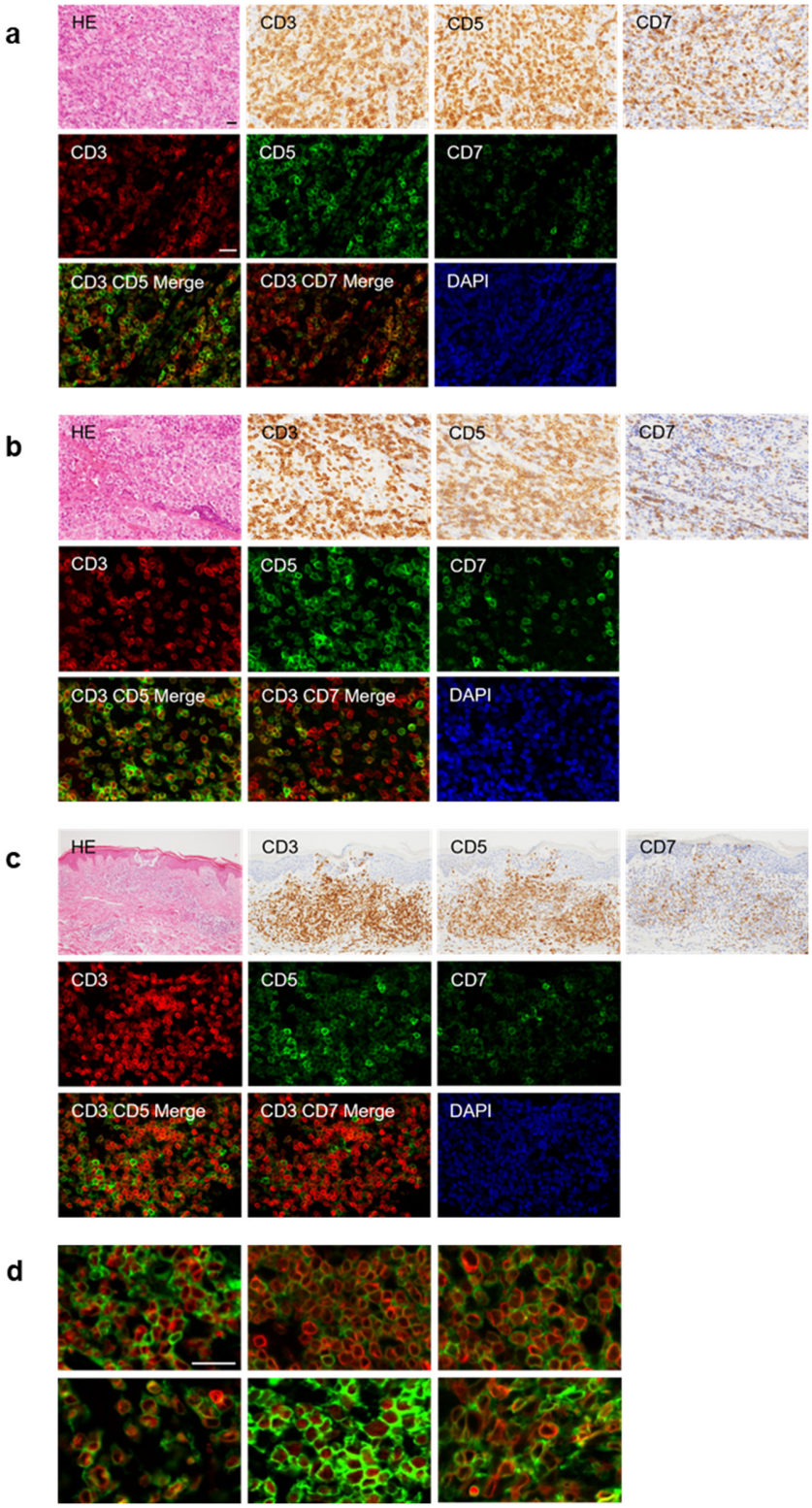
a
HE
CD3
CD5
CD7
CD3
CD5
CD7
CD3 CD5 Merge
CD3 CD7 Merge
DAPI
b
HE
CD3
CD5
CD7
CD3
CD5
CD7
CD3 CD5 Merge
CD3 CD7 Merge
DAPI
c
HE
CD3
CD5
CD7
CD3
CD5
CD7
CD3 CD5 Merge
CD3 CD7 Merge
DAPI
d

Figure 6.

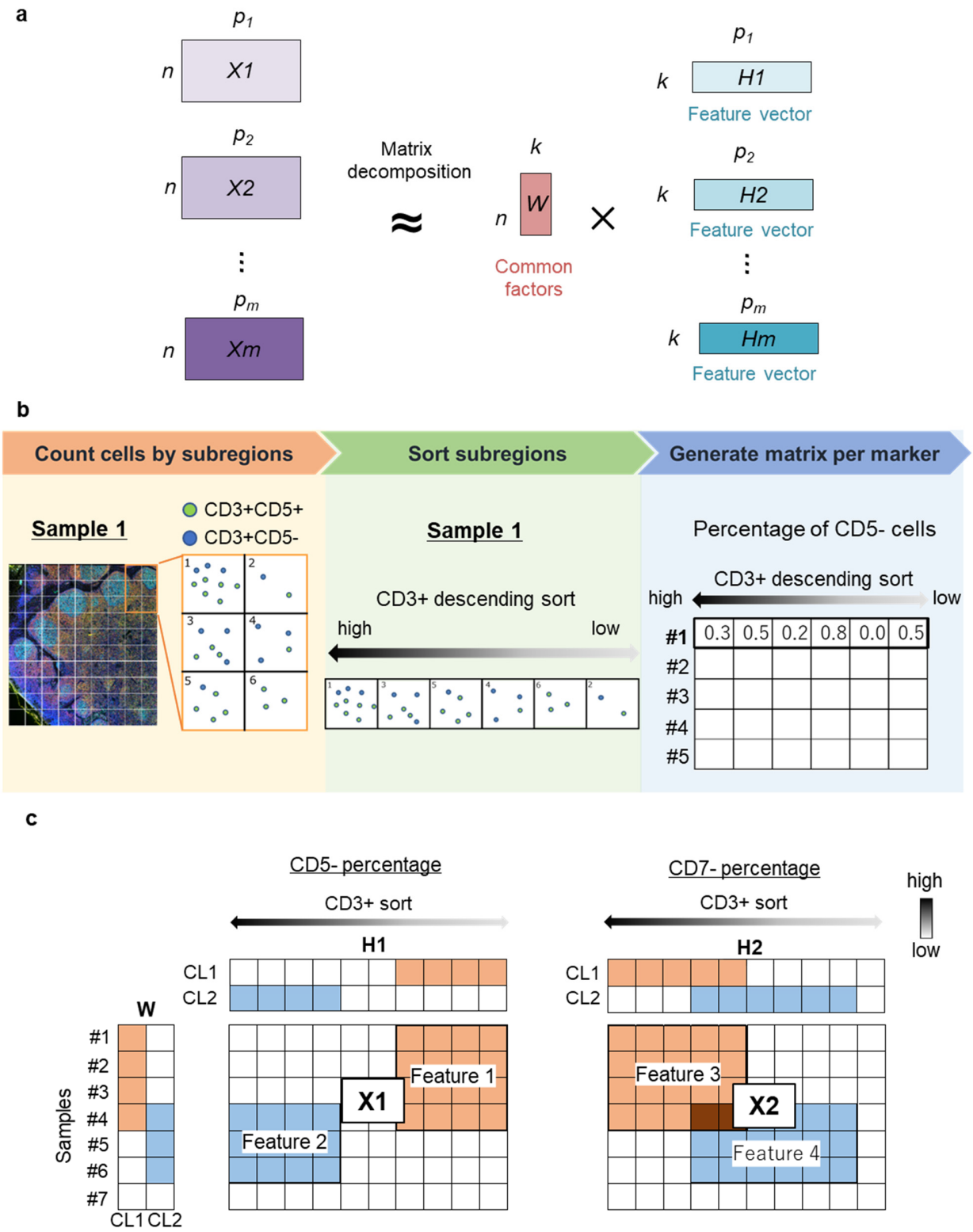
a
Matrix decomposition
Common factors
Feature vector
b
Count cells by subregions
Sort subregions
Generate matrix per marker
Sample 1
CD3+CD5+
CD3+CD5-
CD3+ descending sort
high
low
Percentage of CD5- cells
c
CD5- percentage
CD7- percentage
CD3+ sort
H1
H2
W
X1
X2
Feature 1
Feature 2
Feature 3
Feature 4
Samples
CL1
CL2

Figure 7.

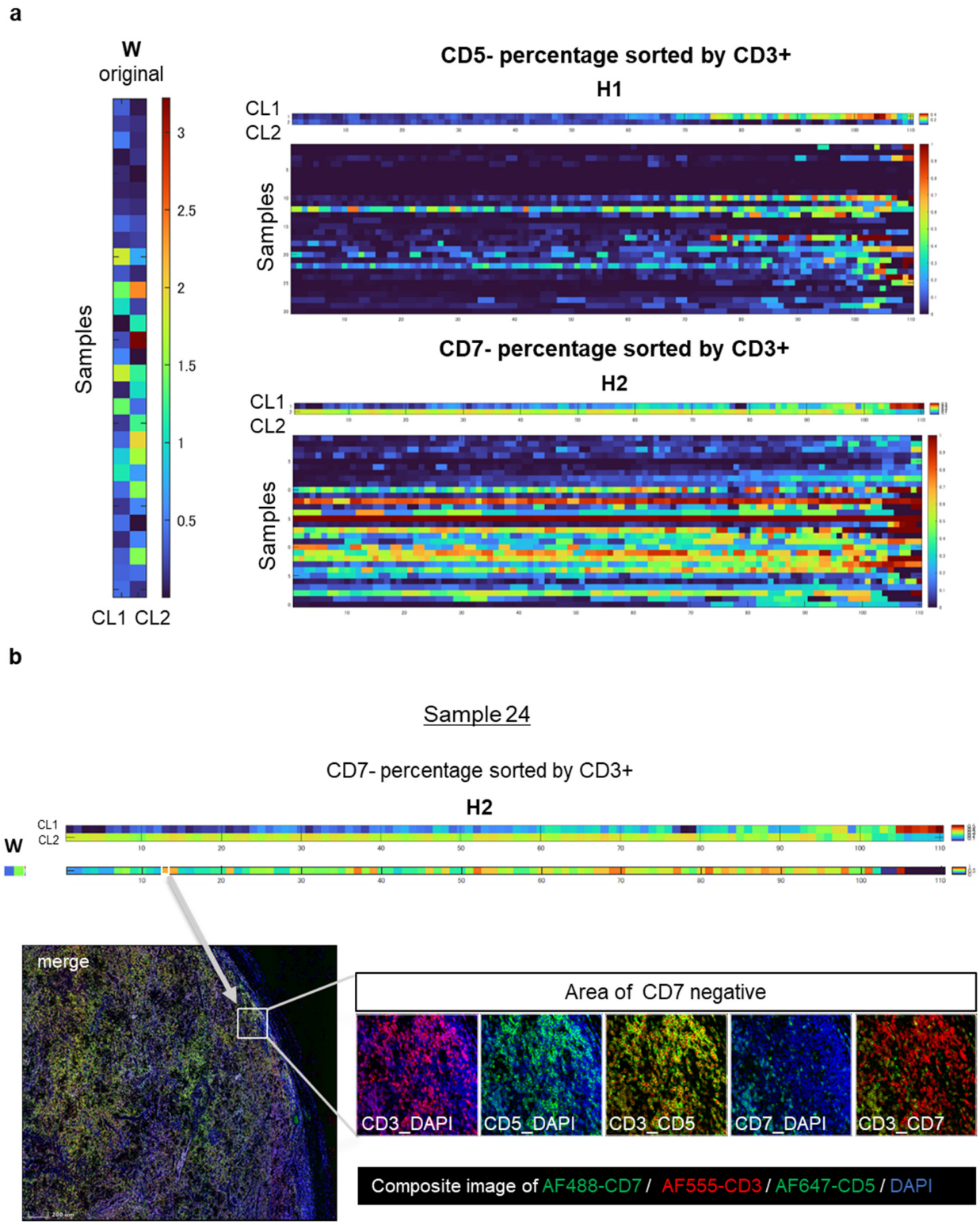
a
W
original
Samples
CL1 CL2
3
2.5
2
1.5
1
0.5
CD5- percentage sorted by CD3+
H1
CL1
CL2
Samples
CD7- percentage sorted by CD3+
H2
CL1
CL2
Samples
b
Sample 24
CD7- percentage sorted by CD3+
H2
W
CL1
CL2
merge
Area of CD7 negative
CD3_DAPI
CD5_DAPI
CD3_CD5
CD7_DAPI
CD3_CD7
Composite image of AF488-CD7 / AF555-CD3 / AF647-CD5 / DAPI

Figure 8.

Tables

Evaluation of stainability of FCM, mIF, and IHC

	CD3, CD5, CD7 expression		FCM
	concordance	discordance	marker deletion (+) cases
mIF	21 (84.0%)	4 (16.0%)	25
IHC	18 (72.0%)	7 (28.0%)	
	CD5 deletion		FCM
	Concordance	discordance	CD5 (-) cases
mIF	5 (83.3%)	1 (16.7%)	6
IHC	3 (50.0%)	3 (50.0%)	
	CD7 deletion		FCM
	concordance	discordance	CD7 (-) cases
mIF	16 (88.9%)	2 (11.1%)	18
IHC	14 (77.8%)	4 (22.2%)	

Evaluation of Cytoplasmic CD3

	mIF		FCM
	Cytoplasmic	Surface	
case	14	2	16
%	87.50%	12.50%	

Table 1. Evaluation of Stainability of FCM, multiplex immunofluorescence (mIF), and IHC.

		Pathological evaluation	
		CD5- or CD7- (Positive)	CD3+CD5+CD7+ (Negative)
jNMF result	CD5- or CD7- (Positive)	**TP** 15	**FP** 2
	CD3+CD5+CD7+ (Negative)	**FN** 1	**TN** 12

Number of Samples	**Sensitivity**	**Specificity**	**Accuracy**
30	**93.75%**	**85.71%**	**90.00%**

Table 2. Correlation Between Pathologist Evaluation and jNMF Results. TP; True positive, FP; False positive, FN; False negative; and TN; True negative.

Figure Legends

Figure 1. Summary of Spectral Imaging-based Single-Step Staining Multiplex Immunofluorescence (SISS-mIF).
(a) Schematic depiction of multiplex direct single-step staining where tissue slides are stained with all fluorophore-conjugated primary antibodies simultaneously. (b) Illustration of spatial sweep spectroscopy, where three-dimensional spectral data are acquired by scanning perpendicular to the line, capturing the fluorescent spectrum of pixels. (c) Overview of image processing, highlighting autofluorescence component spectra extraction via non-negative matrix factorization (NMF) using an unstained slide, and subsequent least square method (LSM) unmixing with the stained matrix from the stained image, incorporating the standard spectral including extracted autofluorescence spectra. (d) Color map representation of antibody quantification, outputting images with antibodies per voxel.

Figure 2. Hyper Spectral Imaging System.
(a) Schematic outline of the hyperspectral imaging system. A custom-made multispectral scanner facilitates the acquisition of data across 135 channels. Four line-shaped beam profiles are employed for excitation, with each laser sequentially scanning the stained sample. The resultant fluorescence is analyzed by a spectrometer, with data captured by an image sensor. (b) Representation of spatio-spectral signals on the image sensor, where spectroscopic fluorescence is captured, displaying spatial information on the horizontal axis and spectroscopic information on the vertical axis.

Figure 3. Spectral Unmixing Algorithms.
(a) Spectra before and after optimization via NMF. Solid lines in the top chart represent five initial autofluorescence spectra inputted into the NMF algorithm (Red: Arachidonic Acid, Lime: Elastin, Blue: FAD, Magenta: PLD, Cyan: Protoporphyrin), while dashed lines in the bottom chart show optimized spectra by the NMF algorithm (Red: Auto Fluorescence1, Lime: Auto Fluorescence2, Blue: Auto Fluorescence3, Cyan: Auto Fluorescence4). The horizontal axis denotes wavelength [CH], and the vertical axis represents intensity [a.u.]. Fluorescence spectra excited by 4-lasers are concatenated along the wavelength direction. (b) Schematic of spectral optimization by NMF. The measured spectral cube data A (Row: fluorescent spectra, Column: pixel) is dimensionally reduced to the fluorescent antibody count element W (Row: fluorophore species, Column: pixel) and the fluorescence spectra element H (Row: wavelength, Column: fluorescent intensity) by optimizing two elements to minimize residuals Δ without allowing negative values. (c) Conceptual diagram for acquiring reference spectra for antibody count. A dispersed sample at a known concentration is measured on a sensor with a defined volume, expressing the number of fluorescent antibodies present in a voxel corresponding to a sensor pixel as [the number of molecules in sensor 1 pix = M × ST × Avogadro number], utilizing the concentration (M) of each dye and the area of one-pixel sensor (S) and the thickness of slide glass (T).

Figure 4. Direct Single-Step Staining Multiplex Immunofluorescence.
(a) Representative 8-plex plus DAPI staining images on human tonsil tissue with merged and composite images showing AF488-CD4 in green, AF555-PD-1 in yellow, AF568-Ki67 in orange, AF647-PD-L1 in red, AF680-CD3 in pink, AF700-CK in white, AF750-CD8 in red-purple, AF790-CD68 in violet, and DAPI in blue. (b) Representative 5-plex plus DAPI staining images on human skin tissue with merged and composite images of AF488-CD45RO in green, AF555-CD3 in yellow, AF647-PD-1 in red, AF680-Sox10 in red-purple, AF750-CK in white, and DAPI in blue. (c) Representative 6-plex plus DAPI staining images on human breast tissue with merged and composite images of AF488-CD4 in green, eFluor (eF) 570-FoxP3 in yellow, eF615-CD20 in light blue, AF647-CD8 in red, AF680-CD68 in red-purple, AF750-CK in white, and DAPI in blue. Scale bars in all images are 50 µm. Deconvolution was applied to all images for image processing.

Figure 5. Image Outputs in Antibody Count.
(a) Representative images captured under various exposure conditions and gain settings, with exposure condition and gain setting in scan condition 1 at 1800 µs and 9 dB, respectively. In scan condition 2, exposure conditions are set to 900 µs, and in scan condition 3, both exposure conditions and the gain are set to 900 µs and 3 dB. Multiplex staining for CD7 (green), CD3 (yellow), and CD5 (red) was performed on serial sections of human tonsils. Scale bars in all images are 50 µm. (b) Graph depicting antibody count values under different exposure conditions, with error bars representing mean ± 1 SD for n = 3. (c) Staining of simplex, duplex, and triplex configurations performed with α-CD3, α-CD3 and α-CD5, α-CD3, α-CD5, and α-CD7, respectively, on serial sections of human tonsil. Scale bars in all images are 50 µm. (d) Graph showing α-CD3 antibody counts in simplex, duplex, and triplex staining configurations, with error bars indicating mean ± 1 SD for n = 3. Deconvolution was applied to all images for image processing.

Figure 6. Detection of CD3, CD5, and CD7 in T-cell Lymphoma.
(a-c) Showcases representative histological, immunohistochemical (IHC), and multiplex immunofluorescence (mIF) images. (a) Depicts a lymph node diagnosed with Angioimmunoblastic T-cell lymphoma (AITL), showing IHC results of CD3(+), CD5(+), and CD7(-) in a mixed population of normal and small T-cells, and corresponding mIF results. Flow cytometry (FCM) results, not displayed, are CD3(-), CD5(+), and CD7(-). (b) Displays another lymph node with an AITL diagnosis, illustrating similar findings in both IHC and mIF results as CD3(+), CD5(+), and CD7(-), with FCM results, also not shown, mirroring the pattern of CD3(-), CD5(+), and CD7(-). (c) Exhibits a skin sample diagnosed with Peripheral T-cell lymphoma (PTCL), showing IHC results of CD3(+), CD5(+), and CD7(-) ranging from negative to weakly positive, and mIF results showing CD3(+), CD5(+), and CD7(-) with dim positive expression. FCM results, though not presented, show CD3(-), CD5(+), and CD7(-) with dim positive expression. (d) Provides representative images of CD3 cytoplasmic expression observed through

mIF, offering a detailed visualization of intracellular protein localization. Scale bars in all images are set at 20 μm to facilitate comparison.

Figure 7. jNMF-Based Spatial Clustering Analysis (jNMF-SCA).
(a) Overview of the jNMF algorithm, illustrating the decomposition of matrices X1, X2, ..., Xm (purple) into a common factor matrix W (red) and m factor matrices H1, H2, ..., Hm (blue) as feature vectors. (b) Data preprocessing flow for jNMF-SCA, detailing the division of the image into small regions of 300 × 300 μm^2, counting positive cells for CD3, CD5, and CD7 in each region, and sorting regions by descending order of CD3(+) cell count. (c) Output image of jNMF-SCA, showing each matrix, X1 as a matrix of CD5 (-) ratio, and X2 as a CD7 (-) ratio. The first column of W corresponds to Cluster 1 (CL1), and the second column to Cluster 2 (CL2). Feature vectors of each cluster, CL1 and CL2, correspond to the first and second rows of H1 and H2, respectively. The orange and blue blocks represent characteristic regions of CL1 and CL2, respectively.

Figure 8. Assisted Diagnosis of T-cell Lymphoma using jNMF-SCA.
(a) Dataset of lymphoma samples and results of jNMF-SCA (W, H), with a heatmap indicating higher values in red and lower values in blue. Regions with a high ratio of CD5 (-) or CD7 (-) appear in red. (b) Field of view with a high proportion of CD7 (-) indicated by jNMF (white box), showing merged and composite images of AF488-CD7 in green, AF555-CD3 in red, AF647-CD5 in green, and DAPI in blue.

Author contributions

T.N., N.K., and T.T. contributed equally to this work. T.N. and K.N. designed and conceived this study. T.K., H.T., developed spectral imaging system. T.N. performed experiments and collected data. T.N., N.K., K.I. M.S. analyzed data. M.K. designed clinical study. T.T. M.I. I.O. M.K. provided clinical samples and clinical information. T.T. I.O. M.K. conducted pathological evaluation and validation. T.N. N.K. T.T. K.I. T.K. M.K. K.N. wrote the manuscript. K.N. supervised the project. All authors have read and agreed to the published version of the manuscript.

Competing interests

T.N., N.K., K.I., M.S., T.K., H.T., K.N. are employees of Sony Corporation. T.T. M.I. I.O. M.K. declares this study was funded by the joint research program between Tokyo Medical and Dental University (TMDU) and Sony corporation.

Acknowledgements

We thank Shuichi Kakuda and Chinatsu Ito for their contribution to staining slides and capturing imaging data.